

High Dimensional Ensemble Kalman Filter

Song Xi Chen*

Department of Statistics and Data Science, Tsinghua University

Hao-Xuan Sun

Center for Big Data Research, Peking University

and

Shouxia Wang

School of Statistics and Management, Shanghai University of Finance and Economics

November 17, 2024

Abstract

The ensemble Kalman Filter (EnKF), as a fundamental data assimilation approach, has been widely used in many fields of earth science, engineering and beyond. However, several theoretical aspects of the EnKF remain unknown, especially when the state variable is of high dimensional accompanied with high resolution observation and physical models. This paper first proposes several high dimensional EnKF (HD-EnKF) methods that provide consistent estimators for the important forecast error covariance and the Kalman gain matrix. It then studies the theoretical properties of the EnKF under both the fixed and high dimensional state variables, which provides the mean square errors of the analysis states to the underlying oracle states offered by the Kalman filter and gives the much needed insight into the roles played by the forecast error covariance on the accuracy of the EnKF. The accuracy of the data assimilation under the misspecified physical model is also considered. Numerical studies on the Lorenz-96 and the Shallow Water Equation models illustrate that the proposed HD-EnKF algorithms perform better than the standard EnKF methods as they provide more robust and accurate assimilated results. The HD-EnKF was applied to assimilate sea temperature in the Northwest Pacific, which showed more accurate out-sample performances than the existing methods.

Keywords: Data Assimilation; Dynamic System; Ensemble Kalman Filter; High Dimensional Imputation.

*The authors contributed equally to this paper and are ordered alphabetically.

1 Introduction

Kalman Filter ([Kalman, 1960](#)) is a fundamental approach for forecasting and data assimilation for a partially observed dynamic system. Data assimilation is a statistical procedure that combines information from numerical physical model forecasts with observed data to obtain the best possible description of a dynamical system and its uncertainty ([Evensen et al., 2022](#)). The assimilated state variables at a time are used to generate the forecast for the next time step. For chaotic systems sensitive to initial values, data assimilation can significantly improve the accuracy of the forecast by using optimized state variables as initial values ([Lorenz, 1963](#)). Although much applied in numerical weather and oceanography prediction, Kalman Filter and its later developments (Ensemble Kalman Filter, three and four-dimensional variational assimilation (3D-Var, 4D-Var; [Pailleux, 1990](#); [Courtier et al., 1998](#))) are the methodological core for scientific algorithms over a range of fields, including hydrology, remote sensing data utilization, carbon data assimilation, robotic control and automatic driving. Data assimilation methods also provide the underlying algorithms and predictive techniques for building digital twins for social and economic systems.

The limitations of the Kalman Filter are (i) it assumes a linear model which is restrictive for many non-linear dynamic systems; and (ii) the forecast error covariance and Kalman gain matrices are expensive to store and update when the dimension of the state vector is large. To overcome these limitations, [Evensen \(1994\)](#) proposed the Ensemble Kalman Filter(EnKF), where the forecast error covariance is estimated by the sample covariance based on generated forecast ensembles. The EnKF only requires storing and operating on much reduced-size state vectors and the ensembles can be generated in parallel. These advantages have made the EnKF an effective and widely used data assimilation scheme.

Estimating the forecast error covariance is a key in the EnKF, which is made in the

EnKF by the sample covariance of the forecast ensembles. Past works on the EnKF found that the sampling error can lead to underestimation of the forecast error covariance and can eventually cause filter divergence (Anderson and Anderson, 1999; Constantinescu et al., 2007). Filter divergence refers to a decreasing ability to correct the ensemble state towards the observations after certain rounds of assimilation. High resolution data assimilation and forecasting techniques are much needed in modern meteorology and atmospheric systems like global carbon calculation and ocean data assimilation, which leads to high dimensional geophysical models with high dimensional state vectors. Besides, along with advances in remote sensing technology in measuring the earth system, there is a growing availability of high spatial resolution satellite observations (Stroud et al., 2010; Guinehut et al., 2012).

The high dimensional state vectors lead to high dimensional forecast error covariance and Kalman gain matrices. The high dimensionality is known to cause the non-convergence of the sample forecast error covariance (Bai and Yin, 1993), which is felt in the form of filter divergence and unreliable data assimilation in practice. Geophysicists have proposed two methods to counter the problems. One is the localization method (Furrer et al., 2006; Furrer and Bengtsson, 2007) that sets covariances to zero if the geographical distances are bigger than a threshold; and the other is the inflation method that enlarges the forecast error covariance by adding either a multiplicative factor or an additive term (Wang and Bishop, 2003; Liang et al., 2012; Constantinescu et al., 2007). However, the statistical properties of these EnKF methods are generally lacking, despite their widespread applications. Katzfuss et al. (2020) proposed Gibbs Ensemble Kalman Filter and Smoother, and particle Ensemble Kalman Filter and Smoother algorithms for high dimensional hierarchical dynamic models from a Bayesian perspective.

This paper proposes several high dimensional EnKF (HD-EnKF) methods based on

consistent high dimensional covariance estimators and conducts a theoretical analysis of assimilated state vectors. It is shown that consistent estimation of the forecast error covariance leads to the consistency of the Kalman gain matrix by establishing an inequality that bounds the error of estimation of the Kalman Gain matrix by that of the forecast error covariance. This implies that, even at the high dimensional setting, the mean square errors (MSEs) of the analysis states by the EnKF could be controlled by the error bounds of the high dimensional forecast error covariance estimators. Thus, consistent recovery of the underlying analysis states can be attained by the proposed HD-EnKF procedure.

We establish the mean square error bounds and weak convergence of the analysis states from the HD-EnKF to the underlying analysis under both fixed and high dimensional cases, as well as for both correct and imperfect physical models. The MSE bounds for the multiple-step forecasting and data assimilation are also provided. Simulation studies suggest that the proposed HD-EnKF algorithm could achieve more accurate and robust assimilation results than the widely used inflation-based EnKF method. We apply the proposed HD-EnKF to assimilate sea temperature by combining a physical ocean model with satellite observations and use the ARGO data to validate the quality of the assimilated sea temperature. Both the simulation and the empirical study showed advantages of the HD-EnKF approach.

The paper is structured as follows. Section 2 reviews the Kalman Filter and the EnKF. Section 3 presents several consistent estimators of the high dimensional forecast error covariance and the key Kalman gain matrix, and establishes the theoretical properties of the EnKF. The effects of imperfect or misspecified models on the accuracy of the EnKF are provided in Section 4. Results of empirical data assimilation based on two well-known geophysical models are reported in Section 5 and the application to the sea temperature

data assimilation is presented in Section 6, followed by a conclusion in Section 7. Details of the proposed HD-EnKF algorithms, additional theoretical and simulation results, and technical details are given in the Supplementary Material (SM).

2 Review on Kalman and Ensemble Kalman Filters

The Kalman Filter (Kalman, 1960) assumes the following linear Gaussian state-space model (which was generalized to nonlinear models in the EnKF)

$$\begin{cases} \mathbf{x}_t = \mathbf{M}_t \mathbf{x}_{t-1} + \mathbf{w}_t, & \mathbf{w}_t \sim N_p(\mathbf{0}, \mathbf{Q}_t), \\ \mathbf{y}_t = \mathbf{H}_t \mathbf{x}_t + \boldsymbol{\varepsilon}_t, & \boldsymbol{\varepsilon}_t \sim N_q(\mathbf{0}, \mathbf{R}_t), \end{cases} \quad (2.1)$$

where \mathbf{x}_t is the p -dimensional not fully observed state vector of a dynamic system at time t , \mathbf{M}_t is the linear model operator (also called evolution or forecast operator), \mathbf{w}_t is the model error term with \mathbf{Q}_t as its covariance, \mathbf{y}_t is the q -dimensional observation vector at time t , \mathbf{H}_t is a linear observation operator which relates the state \mathbf{x}_t to the observation \mathbf{y}_t , and $\boldsymbol{\varepsilon}_t$ is the observation error with \mathbf{R}_t being its covariance matrix.

Assuming \mathbf{M}_t , \mathbf{Q}_t , \mathbf{H}_t , and \mathbf{R}_t are known, the Kalman Filter provides a two-step alternative updating framework based on the theory of multivariate normal distribution. In the forecast step, suppose that $\mathbf{x}_{t-1} \mid \mathbf{y}_{1:t-1} \sim N_p(\mathbf{x}_{t-1}^a, \boldsymbol{\Sigma}_{t-1}^a)$, where \mathbf{x}_{t-1}^a is the analysis state vector at the previous time $t-1$ and $\mathbf{y}_{1:t-1}$ denotes the observation $\{\mathbf{y}_i\}_{i=1}^{t-1}$ up to time $t-1$, the conditional distribution of \mathbf{x}_t given $\mathbf{y}_{1:t-1}$ is

$$\mathbf{x}_t \mid \mathbf{y}_{1:t-1} \sim N_p(\mathbf{x}_t^f, \boldsymbol{\Sigma}_t^f) \equiv N_p(\mathbf{M}_t \mathbf{x}_{t-1}^a, \mathbf{M}_t \boldsymbol{\Sigma}_{t-1}^a \mathbf{M}_t^T + \mathbf{Q}_t), \quad (2.2)$$

where $\mathbf{x}_t^f = \mathbf{M}_t \mathbf{x}_{t-1}^a$ is the forecast state and

$$\boldsymbol{\Sigma}_t^f = \mathbf{M}_t \boldsymbol{\Sigma}_{t-1}^a \mathbf{M}_t^T + \mathbf{Q}_t, \quad (2.3)$$

is the variance of the forecast error $\mathbf{x}_t - \mathbf{x}_t^f$, also called the forecast error covariance matrix.

In the update (assimilation) step, the goal is to update \mathbf{x}_t^f according to the new observation \mathbf{y}_t and to reduce the difference between the true state \mathbf{x}_t and the forecast state \mathbf{x}_t^f . The joint distribution of $(\mathbf{x}_t, \mathbf{y}_t)$ given $\mathbf{y}_{1:t-1}$ is Gaussian, which implies that

$$\mathbf{x}_t \mid \mathbf{y}_{1:t} \sim N_p(\mathbf{x}_t^a, \Sigma_t^a), \quad (2.4)$$

where, by the conditional Gaussian distribution formulae,

$$\mathbf{x}_t^a = \mathbf{x}_t^f + \mathbf{K}_t(\mathbf{y}_t - \mathbf{H}_t\mathbf{x}_t^f), \quad \Sigma_t^a = (\mathbf{I}_p - \mathbf{K}_t\mathbf{H}_t) \Sigma_t^f \quad \text{and} \quad (2.5)$$

$$\mathbf{K}_t = \Sigma_t^f \mathbf{H}_t^\top (\mathbf{H}_t \Sigma_t^f \mathbf{H}_t^\top + \mathbf{R}_t)^{-1}, \quad (2.6)$$

which are, respectively, the analysis (assimilation) state and the associated analysis covariance matrix, and the Kalman gain matrix. Note that the analysis state \mathbf{x}_t^a is the minimum variance unbiased estimator for the mean of \mathbf{x}_t under the linear state-space model (2.1).

However, models in earth science or engineering are often nonlinear, that is the evolution model in (2.1) may not be linear so that $\mathbf{x}_t = \mathcal{M}_t(\mathbf{x}_{t-1}) + \mathbf{w}_t$, where \mathcal{M}_t is a nonlinear model operator that can invalidate the forecast distribution in (2.2). Besides, for large dynamic systems, the dimension p of the state vector \mathbf{x}_t can be large so that the forecast error covariance Σ_t^f is expensive to compute and store. To tackle these problems, Evensen (1994) proposed the EnKF, where the forecast error covariance is no longer updated as (2.3) but by the sample covariance based on n forecast ensembles. It hence only needs to store and operate on n vectors of dimension p , and is convenient for parallel computing.

The EnKF assumes possibly nonlinear model system with linear observation operator:

$$\begin{cases} \mathbf{x}_t = \mathcal{M}_t(\mathbf{x}_{t-1}) + \mathbf{w}_t, & \mathbf{w}_t \sim N_p(\mathbf{0}, \mathbf{Q}_t), \\ \mathbf{y}_t = \mathbf{H}_t\mathbf{x}_t + \varepsilon_t, & \varepsilon_t \sim N_q(\mathbf{0}, \mathbf{R}_t), \end{cases} \quad (2.7)$$

where \mathcal{M}_t is the possibly nonlinear model operator, \mathbf{H}_t is a linear observation operator. It further assumes that the forecast error $\boldsymbol{\eta}_t = \mathbf{x}_t - \mathbf{x}_t^f$ follows a Gaussian distribution given

$\mathbf{y}_{1:t-1}$, that is $\mathbf{x}_t - \mathbf{x}_t^f \mid \mathbf{y}_{1:t-1} \sim N_p(\mathbf{0}, \boldsymbol{\Sigma}_t^f)$, where $\mathbf{x}_t^f = \mathbb{E}(\mathbf{x}_t \mid \mathbf{y}_{1:t-1})$. Here \mathcal{M}_t , \mathbf{H}_t , and \mathbf{R}_t are assumed to be known for the time being as in the Kalman Filter.

A key feature of the EnKF is to generate an ensemble of perturbed forecast states $\{\mathbf{x}_{t,j}^f\}_{j=1}^n$ of size n from the conditional distribution of \mathbf{x}_t given $\mathbf{y}_{1:t-1}$, which are used to estimate the forecast error covariance matrix $\boldsymbol{\Sigma}_t^f$. Given the analysis ensemble at the previous time step $\{\mathbf{x}_{t-1,j}^a\}_{j=1}^n$, the EnKF consists of the following three steps.

Step (i): Run the model forward in time to get the perturbed forecast state and their average:

$$\mathbf{x}_{t,j}^f = \mathcal{M}_t(\mathbf{x}_{t-1,j}^a) + \mathbf{w}_{t,j} \text{ and } \hat{\mathbf{x}}_t^f = n^{-1} \sum_{j=1}^n \mathbf{x}_{t,j}^f, \text{ where } \mathbf{w}_{t,j} \stackrel{IID}{\sim} N_p(\mathbf{0}, \mathbf{Q}_t). \quad (2.8)$$

Step (ii): Estimate the forecast error covariance matrix $\boldsymbol{\Sigma}_t^f$ by the sample covariance matrix of the forecast ensemble, namely

$$\hat{\boldsymbol{\Sigma}}_t^f = (n-1)^{-1} \sum_{j=1}^n (\mathbf{x}_{t,j}^f - \hat{\mathbf{x}}_t^f)(\mathbf{x}_{t,j}^f - \hat{\mathbf{x}}_t^f)^\top \triangleq \mathbf{S}_t^f, \quad (2.9)$$

and obtain an estimate of the Kalman gain matrix $\hat{\mathbf{K}}_t = \hat{\boldsymbol{\Sigma}}_t^f \mathbf{H}_t^\top (\mathbf{H}_t \hat{\boldsymbol{\Sigma}}_t^f \mathbf{H}_t^\top + \mathbf{R}_t)^{-1}$.

Step (iii): Calculate the perturbed residuals $\mathbf{d}_{t,j} = \mathbf{y}_t + \boldsymbol{\varepsilon}_{t,j} - \mathbf{H}_t \mathbf{x}_{t,j}^f$ where $\{\boldsymbol{\varepsilon}_{t,j}\}_{j=1}^n \stackrel{IID}{\sim} N(\mathbf{0}, \mathbf{R}_t)$, and let $\mathbf{d}_t = n^{-1} \sum_{j=1}^n \mathbf{d}_{t,j}$. Compute the perturbed analysis states and their average, the assimilated (analysis) state,

$$\begin{aligned} \mathbf{x}_{t,j}^a &= \mathbf{x}_{t,j}^f + \hat{\boldsymbol{\Sigma}}_t^f \mathbf{H}_t^\top (\mathbf{H}_t \hat{\boldsymbol{\Sigma}}_t^f \mathbf{H}_t^\top + \mathbf{R}_t)^{-1} \mathbf{d}_{t,j}, \\ \hat{\mathbf{x}}_t^a &= \frac{1}{n} \sum_{j=1}^n \mathbf{x}_{t,j}^a = \hat{\mathbf{x}}_t^f + \hat{\boldsymbol{\Sigma}}_t^f \mathbf{H}_t^\top (\mathbf{H}_t \hat{\boldsymbol{\Sigma}}_t^f \mathbf{H}_t^\top + \mathbf{R}_t)^{-1} \mathbf{d}_t, \end{aligned} \quad (2.10)$$

which will be used for the data assimilation at the next time step.

The EnKF does not require the expensive recursions (2.3) and (2.5)-(2.6) used in the Kalman Filter. Instead, it estimates the forecast error covariance $\boldsymbol{\Sigma}_t^f$ by the sample covariance. For the case with non-linear model operator as in (2.7), we can still define the underlying analysis state \mathbf{x}_t^a by (2.5)-(2.6), where $\mathbf{x}_t^f = \mathbb{E}(\mathbf{x}_t \mid \mathbf{y}_{1:t-1}) = \mathbb{E}(\mathcal{M}_t(\mathbf{x}_{t-1}) + \mathbf{w}_t \mid \mathbf{y}_{1:t-1})$

is the forecast state and Σ_t^f is the forecast error covariance defined by $\Sigma_t^f = \text{var}((\mathbf{x}_t - \hat{\mathbf{x}}_t^f) \mid \mathbf{y}_{1:t-1})$. In fact, \mathbf{x}_t^a defined by (2.5)-(2.6) is the solution to the minimizing problem (2.11)

$$J(\mathbf{x}) = \frac{1}{2} \{ (\mathbf{x} - \hat{\mathbf{x}}_t^f)^T (\hat{\Sigma}_t^f)^{-1} (\mathbf{x} - \hat{\mathbf{x}}_t^f) + (\mathbf{y}_t - \mathbf{H}_t \mathbf{x})^T \mathbf{R}_t^{-1} (\mathbf{y}_t - \mathbf{H}_t \mathbf{x}) \} \quad (2.11)$$

with $\hat{\mathbf{x}}_t^f$ and $\hat{\Sigma}_t^f$ replaced by \mathbf{x}_t^f and Σ_t^f . For the ease of reference, and to avoid differentiating between the linear and the non-linear cases, we also call \mathbf{x}_t^a as the analysis state of the Kalman Filter even in the non-linear model case. The next two sections will establish the convergence of the EnKF analysis state $\hat{\mathbf{x}}_t^a$ to the underlying \mathbf{x}_t^a of the Kalman Filter.

3 Convergence of Ensemble Kalman Filter

We first provide the upper bound of the estimation error of the estimated Kalman gain matrix. Throughout the paper, $\|\cdot\|$ denotes the L_2 (spectral) norm of a matrix or the L_2 norm of a vector, while other matrix norms will be specified explicitly. For two positive sequences a_n and b_n , $a_n \asymp b_n$, $a_n \ll b_n$ and $a_n \gg b_n$ mean that a_n/b_n is bounded away from zero and infinity, $a_n/b_n \rightarrow 0$ and $b_n/a_n \rightarrow 0$ as $n \rightarrow \infty$, respectively. The following assumptions are needed in the analysis.

Assumption 1. (i) The model operator \mathcal{M}_t is Lipschitz continuous, that is $\|\mathcal{M}_t(\mathbf{x}) - \mathcal{M}_t(\mathbf{x}')\| \leq \ell_0 \|\mathbf{x} - \mathbf{x}'\|$ for any $\mathbf{x}, \mathbf{x}' \in R^p$ for a positive constant ℓ_0 . (ii) The model operator \mathcal{M}_t can be locally linearized and satisfies $\|\mathcal{M}_t(\mathbf{x}) - \mathcal{M}_t(\mathbf{x}')\| \leq \|\dot{M}_t\| \|\mathbf{x} - \mathbf{x}'\|$ for $\mathbf{x}, \mathbf{x}' \in R^p$ and $\|\mathbf{x} - \mathbf{x}'\| \leq \|\mathbf{h}\|$ for a small positive \mathbf{h} , where \dot{M}_t is a matrix related to the linear expansion of \mathcal{M}_t at \mathbf{x} and $\|\dot{M}_t\| \leq \ell_t$ for some positive constants ℓ_t .

Assumption 2. The model error covariance \mathbf{Q}_t , the observation error covariance \mathbf{R}_t and the initial analysis covariance Σ_0^a satisfy $0 < \varepsilon_0 \leq \lambda_{\min}(\mathbf{Q}_t) \leq \lambda_{\max}(\mathbf{Q}_t) \leq 1/\varepsilon_0$, $0 < \varepsilon_0 \leq \lambda_{\min}(\mathbf{R}_t) \leq \lambda_{\max}(\mathbf{R}_t) \leq 1/\varepsilon_0$, and $\lambda_{\max}(\Sigma_0^a) \leq 1/\varepsilon_0$, for a positive ε_0 , respectively, where

λ_{\max} and λ_{\min} are the maximum and minimum eigenvalue operators, respectively.

Assumption 3. The observation operator \mathbf{H}_t satisfies $\|\mathbf{H}_t\| \leq C$ for a constant $C > 0$.

Assumption 1 (i) and (ii) are two versions of the condition on the model operator \mathcal{M}_t . If model \mathcal{M}_t is linear, it automatically satisfies both (i) and (ii) of Assumption 1. If \mathcal{M}_t is nonlinear and Lipschitz continuous, $\mathcal{M}_t(\cdot)$ has at most linear growth at infinite interval. However, strongly nonlinear systems may not satisfy the Lipschitz condition. In that case, we assume \mathcal{M}_t satisfies condition (ii), which is related to the tangent linear hypothesis (Thepaut and Courtier, 1991; Bouttier and Courtier, 1999) in the 4D-Var, where \mathcal{M}_t is determined in the linear approximation $\mathcal{M}_t(\mathbf{x}_t + \mathbf{h}) \approx \mathcal{M}_t(\mathbf{x}_t) + \dot{M}_t \mathbf{h}$ in the vicinity of \mathbf{x}_t for a perturbation \mathbf{h} , and the operator \dot{M}_t is called the differential or tangent linear function of \mathcal{M}_t at point \mathbf{x}_t . Assumption 2 assumes the eigenvalues of the three basic covariances \mathbf{Q}_t , \mathbf{R}_t and Σ_0^a are bounded away from zero and infinity. From Lemma S.3.1 of the SM, the eigenvalues of Σ_t^f satisfy the conditions for the thresholding and bandable(or circular bandable) covariance classes under Assumption 2 and Assumptions 1-2, respectively. Assumption 3 puts a mild condition on the observation operator \mathbf{H}_t .

The following proposition provides a basic result that bounds $\|\hat{\mathbf{K}}_t - \mathbf{K}_t\|$ for both fixed and high dimensional situations, where $\hat{\mathbf{K}}_t = \hat{\Sigma}_t^f \mathbf{H}_t^\top (\mathbf{H}_t \hat{\Sigma}_t^f \mathbf{H}_t^\top + \mathbf{R}_t)^{-1}$ is an estimator of the Kalman gain matrix assuming \mathbf{R}_t is known.

Proposition 3.1. *Suppose Assumption 2 holds and $\lambda_{\min}(\mathbf{R}_t) \geq \varepsilon_0$ for a positive ε_0 ,*

$$\|\hat{\mathbf{K}}_t - \mathbf{K}_t\| \leq \lambda_{\min}^{-1}(\mathbf{R}_t) \|\mathbf{I} - \mathbf{K}_t \mathbf{H}_t\| \|\mathbf{H}_t\| \|\hat{\Sigma}_t^f - \Sigma_t^f\| \leq \lambda_{\min}^{-1}(\mathbf{R}_t) \|\mathbf{H}_t\| \|\hat{\Sigma}_t^f - \Sigma_t^f\|.$$

The last inequality is derived from $\|\mathbf{I} - \mathbf{K}_t \mathbf{H}_t\| < 1$ as $(\mathbf{I} - \mathbf{K}_t \mathbf{H}_t) \Sigma_t^f = \Sigma_t^a$ is the variance of $\mathbf{x}_t | \mathbf{y}_{1:t}$ and $(\mathbf{I} - \mathbf{K}_t \mathbf{H}_t) \Sigma_t^f = \Sigma_t^a < \Sigma_t^f$ as long as \mathbf{x}_t is correlated with $\mathbf{y}_{1:t}$. Proposition 3.1 suggests that the upper bound of the estimation error in $\|\hat{\mathbf{K}}_t - \mathbf{K}_t\|$ mainly depends

on the bound of $\|\hat{\Sigma}_t^f - \Sigma_t^f\|$. Proposition 3.1 holds under weak conditions and actually is valid for both fixed and high dimensions. Note that under fixed dimension, the sample covariance is consistent with the underlying population covariance at the \sqrt{n} rate, that is $\|\hat{\Sigma}_t^f - \Sigma_t^f\| = O_P(n^{-1/2})$ and thus $\|\hat{\mathbf{K}}_t - \mathbf{K}_t\| = O_P(n^{-1/2})$. The results for the high dimensions are shown later. In practice, the true observation error covariance matrix \mathbf{R}_t may be unknown. Corollary S.3.1 of the SM provides an upper bound of the estimation error of the $\hat{\mathbf{K}}_t$ to \mathbf{K}_t when both Σ_t^f and \mathbf{R}_t are estimated by $\hat{\Sigma}_t^f$ and $\hat{\mathbf{R}}_t$, respectively.

Based on the result in Proposition 3.1, we can establish the convergence of the EnKF forecast and analysis states $\hat{\mathbf{x}}_t^f$ and $\hat{\mathbf{x}}_t^a$ to their oracle Kalman Filter counterparts \mathbf{x}_t^f and \mathbf{x}_t^a based on the true Σ_t^f and the true underlying evolution given in (2.5)-(2.6) by firstly establishing the convergence of $\hat{\Sigma}_t^f$ to Σ_t^f . For the fixed dimension case, the sample covariance matrix is consistent such that $\|\hat{\Sigma}_t^f - \Sigma_t^f\| = O_P(n^{-1/2})$. However, when the dimension p of the state vector \mathbf{x}_t is high so that $p \gg n$, the forecast ensemble sample covariance $\hat{\Sigma}_t^f$ in (2.9) is no longer consistent to the underlying covariance Σ_t^f (Bai and Yin, 1993), which is a major threat to the validity of the EnKF method.

Next, we present several consistent estimators of the high dimensional forecast error covariance Σ_t^f and their covariance classes before we give the convergence of the EnKF.

3.1 Consistent estimation of high dimensional Σ_t^f

The banding estimator (Bickel and Levina, 2008b) of the forecast error covariance matrix with bandwidth k is $B_k(\mathbf{S}_t^f) = [s_{tij}^f \mathbf{1}(|i-j| \leq k)]$, where $0 \leq k < p$ and $\mathbf{S}_t^f = [s_{tij}^f]_{p \times p}$ is the sample covariance of the EnKF forecast ensembles. The covariance matrix class suitable for the banding estimator is the following bandable covariance class, $\mathcal{U}_b(\varepsilon_0, \alpha, C) = \{\Sigma = (\sigma_{ij})_{p \times p} : \max_j \sum_{|i-j| > k} |\sigma_{ij}| \leq Ck^{-\alpha} \text{ for all } k > 0 \text{ and } 0 < \varepsilon_0 \leq \lambda_{\min}(\Sigma) \leq \lambda_{\max}(\Sigma) \leq$

$1/\varepsilon_0\}$ for some positive α , C and ε_0 . This bandable pattern is generally consistent with the dependence between variables observed at sites i and j in geoscience studies, as the dependence becomes weaker as the distance between the two sites gets larger.

The banding estimator administrates a hard threshold as it sets all matrix elements beyond the k -th sub-diagonals to zero. [Cai et al. \(2010\)](#) updated the banding estimator with a tapering alteration which tapers down the level of the thresholding gradually

$$\hat{\Sigma}_{t,tap}^f(k) = \mathbf{S}_t^f \circ \mathbf{W}(k) = (w_{ij}(k)s_{tij}^f)_{p \times p},$$

where $\mathbf{W}(k) = (w_{ij}(k))_{p \times p}$, with $w_{ij}(k) = (2/k) \{(k - |i - j|)_+ - (k/2 - |i - j|)_+\}$, is the tapering matrix at a tapering width k which is usually an even integer and $1 \leq k \leq p$.

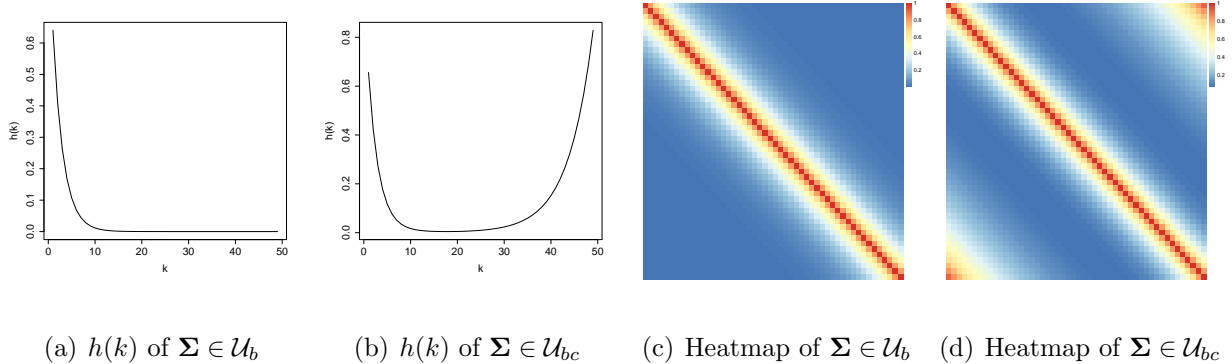


Figure 1: Bandable and circular bandable covariance matrices: the average energy function $h(k)$ in Panels (a) and (b) and their heatmaps in Panels (c) and (d), where $h(k)$ is the average of the squares of the k^{th} sub-diagonal entries.

In earth science, due to the largely spherical shape of the earth, for a study region that encompasses the entire earth or its poles, the state vectors are highly dependent for the variable components between the two ends of the state vector. Thus we propose a circular form of the bandable structure, $\mathcal{U}_{bc}(\varepsilon_0, \alpha, C) = \{\Sigma = (\sigma_{ij})_{p \times p} : \max_j \sum_{k_1 < |i-j| < p-k_2} |\sigma_{ij}| \leq C(k_1 + k_2)^{-\alpha} \text{ for all } 0 < k_1, k_2 < p \text{ and } 0 < \varepsilon_0 \leq \lambda_{\min}(\Sigma) \leq \lambda_{\max}(\Sigma) \leq 1/\varepsilon_0\}$. Figure 1 depicts the $h(k)$ functions and heatmaps of two specific covariance matrices that belong to the two bandable covariance classes \mathcal{U}_b and \mathcal{U}_{bc} , where $h(k)$ is the average of the squares

of the k^{th} subdiagonal entries of a covariance defined by $h(k) := \frac{1}{2(p-k)} \sum_{|l_1-l_2|=k} \sigma_{l_1 l_2}^2 = \frac{1}{p-k} \sum_{l=1}^{p-k} \sigma_{l+l}^2$. Figures 1 (a)-(b) show that the $h(k)$ function of covariances in \mathcal{U}_b is a L -type curve as the subdiagonal index k increases, while it is an U -type curve for covariances in \mathcal{U}_{bc} . For covariances in the circular bandable class $\mathcal{U}_{bc}(\varepsilon_0, \alpha, C)$, the proposed mid-banding forecast error covariance estimator with bandwidths k_1 and k_2 is $B_{k_1, k_2}(\mathbf{S}_t^f) = [s_{ij}^f \mathbf{1}(|i-j| \leq k_1 \text{ or } |i-j| \geq (p-k_2))]$, where $0 \leq k_1 < (p-k_2) \leq p$.

The bandable matrix class requires that the state vector \mathbf{x}_t has an ordering (or a permutation) such that the correlation decays as two components of \mathbf{x}_t are further apart. However, the presence of geo-spatial processes (weather front or hurricane) and geography (mountains or ocean) will interrupt the spatial dependence ordering prescribed by the banding covariance class. In such situations, the thresholding covariance class $\mathcal{U}_\tau(\gamma, c_0(p), M, \varepsilon_0)$ suitable for the thresholding estimator (Bickel and Levina, 2008a) may be employed, where $\mathcal{U}_\tau(\gamma, c_0(p), M, \varepsilon_0) = \{\Sigma = (\sigma_{ij})_{p \times p} : \sigma_{ii} \leq M, \sum_{j=1}^p |\sigma_{ij}|^\gamma \leq c_0(p), \text{ for all } i \text{ and } \lambda_{\min}(\Sigma) \geq \varepsilon_0 > 0\}$, for $0 \leq \gamma < 1$. The thresholding forecast error covariance matrix estimator with a threshold level s is $T_s(\mathbf{S}_t^f) = [s_{ij}^f \mathbf{1}(|s_{ij}^f| \geq s)]$.

Note that all of the banding, mid-banding, tapering and thresholding estimators depend on either the bandwidth k or the threshold s which can be selected by methods in Qiu and Chen (2015). For the bandwidths k_1, k_2 of the mid-banding estimator, we propose a similar selection method and details can be found in Section S.2 of the SM.

The following Proposition 3.2 summarizes the convergence rates of the forecast error covariance estimators by the banding, mid-banding, tapering and thresholding methods.

Proposition 3.2. *Suppose the forecast ensemble $\{\mathbf{x}_{ti}^f\}_{i=1}^n$ are conditionally IID Gaussian or sub-exponentially distributed as in Assumption S.3.1 of the SM.*

(i) *For the banding estimator $B_k(\mathbf{S}_t^f)$ with $k \asymp (n^{-1} \log p)^{-1/(2(\alpha+1))}$, then uniformly for*

$$\boldsymbol{\Sigma}_t^f \in \mathcal{U}_b(\varepsilon_0, \alpha, C), \mathbb{E}\|B_k(\mathbf{S}_t^f) - \boldsymbol{\Sigma}_t^f\|^2 \asymp (n^{-1}\log p)^{\alpha/(\alpha+1)}.$$

(ii) For the mid-banding estimator $B_{k_1, k_2}(\mathbf{S}_t^f)$ with $k_1 + k_2 \asymp (n^{-1}\log p)^{-1/(2(\alpha+1))}$, then uniformly on $\boldsymbol{\Sigma}_t^f \in \mathcal{U}_{bc}(\varepsilon_0, \alpha, C)$, $\mathbb{E}\|B_{k_1, k_2}(\mathbf{S}_t^f) - \boldsymbol{\Sigma}_t^f\|^2 \asymp (n^{-1}\log p)^{\alpha/(\alpha+1)}$.

(iii) For the tapering estimator $\hat{\boldsymbol{\Sigma}}_{t, \text{tap}}^f(k)$, suppose $\{\mathbf{x}_{ti}^f\}_{i=1}^n$ are sub-Gaussian, then for $\boldsymbol{\Sigma}_t^f \in \mathcal{U}_b(\varepsilon_0, \alpha, C)$, $\mathbb{E}\|\hat{\boldsymbol{\Sigma}}_{t, \text{tap}}^f(k) - \boldsymbol{\Sigma}_t^f\|^2 \asymp \min\{n^{-2\alpha/(2\alpha+1)} + n^{-1}\log p, n^{-1}p\}$.

(iv) For the thresholding estimator $T_s(\mathbf{S}_t^f)$, for sufficiently large M' , if $s = M'(n^{-1}\log p)^{-1/2}$, then, uniformly on $\mathcal{U}_\tau(\gamma, c_0(p), M)$, $\mathbb{E}\|T_s(\mathbf{S}_t^f) - \boldsymbol{\Sigma}_t^f\|^2 \asymp c_0^2(p) (n^{-1}\log p)^{(1-\gamma)}$.

The results in Proposition 3.2 (i), (iii) and (iv) are, respectively, from [Bickel and Levina \(2008b\)](#), [Cai et al. \(2010\)](#) and [Bickel and Levina \(2008a\)](#). And that for the mid-banding estimator in Proposition 3.2 (ii) is a new result whose proof is given in the SM. They imply that the high dimensional covariance estimators are consistent to $\boldsymbol{\Sigma}_t^f$ under the spectral norm if $\log(p) = o(n)$ or $p = o(e^{cn})$ for any positive constant c .

According to Proposition 3.1, the convergence results in Proposition 3.2 on the high dimensional estimation of $\boldsymbol{\Sigma}_t^f$ translate to that of the estimated Kalman Gain $\hat{\mathbf{K}}_t = \hat{\boldsymbol{\Sigma}}_t^f \mathbf{H}_t^\top (\mathbf{H}_t \hat{\boldsymbol{\Sigma}}_t^f \mathbf{H}_t^\top + \mathbf{R}_t)^{-1}$ to \mathbf{K}_t . Specifically,

$$\begin{aligned} \text{if } \boldsymbol{\Sigma}_t^f \in \mathcal{U}_b(\varepsilon_0, \alpha, C) \text{ or } \mathcal{U}_{bc}(\varepsilon_0, \alpha, C), \mathbb{E}\|\hat{\mathbf{K}}_t - \mathbf{K}_t\|^2 &\asymp (n^{-1}\log p)^{\frac{\alpha}{\alpha+1}} \text{ for } \hat{\boldsymbol{\Sigma}}_t^f = B_k(\mathbf{S}_t^f) \text{ or } B_{k_1, k_2}(\mathbf{S}_t^f); \\ \text{if } \boldsymbol{\Sigma}_t^f \in \mathcal{U}_b(\varepsilon_0, \alpha, C), \mathbb{E}\|\hat{\mathbf{K}}_t - \mathbf{K}_t\|^2 &\asymp \min\{n^{-2\alpha/(2\alpha+1)} + n^{-1}\log p, n^{-1}p\} \text{ for } \hat{\boldsymbol{\Sigma}}_t^f = \hat{\boldsymbol{\Sigma}}_{t, \text{tap}}^f(k); \\ \text{if } \boldsymbol{\Sigma}_t^f \in \mathcal{U}_\tau(\gamma, c_0(p), M), \mathbb{E}\|\hat{\mathbf{K}}_t - \mathbf{K}_t\|^2 &\asymp c_0^2(p) (n^{-1}\log p)^{(1-\gamma)} \text{ for } \hat{\boldsymbol{\Sigma}}_t^f = T_s(\mathbf{S}_t^f). \end{aligned} \quad (3.1)$$

As will be shown in the following, the estimation error of the Kalman gain matrix $\Delta_{\mathbf{K}, t} = \mathbb{E}\|\hat{\mathbf{K}}_t - \mathbf{K}_t\|^2$ plays a crucial role in quantifying the effects of the high dimensional banding, the mid-banding, the tapering and the thresholding estimators for $\boldsymbol{\Sigma}_t^f$.

3.2 Convergence of High Dimensional Ensemble Kalman Filter

When the dimension p of \mathbf{x}_t is high, to allow consistency of the data assimilation, we have to use the high dimensional covariance estimators in Section 3.1 for the forecast error covariance matrix Σ_t^f and the Kalman Gain matrix \mathbf{K}_t . Based on the consistent estimators of Σ_t^f and \mathbf{K}_t , we propose the HD-EnKF algorithms given in Section S.1 of the SM and we establish the accuracy of the assimilated state $\hat{\mathbf{x}}_t^a$ to the underlying \mathbf{x}_t^a . To simplify notation, we denote $\Delta_{\mathbf{K},k} = \mathbb{E}\|\hat{\mathbf{K}}_k - \mathbf{K}_k\|^2$ and

$$\begin{aligned} \Omega_t &= \text{tr} \left(n^{-1} \mathbb{E}(\hat{\mathbf{K}}_t - \mathbf{K}_t)^\top (\hat{\mathbf{K}}_t - \mathbf{K}_t) (\mathbf{H}_t \Sigma_t^f \mathbf{H}_t^\top + \mathbf{R}_t) \right) + \mathbb{E} \| (\hat{\mathbf{K}}_t - \mathbf{K}_t) (\mathbf{y}_t - \mathbf{H}_t \mathbf{x}_t^f) \|^2 \\ &\quad - 2 \text{tr} \left((\mathbf{I} - \mathbf{K}_t \mathbf{H}_t)^\top \mathbb{E}(\hat{\mathbf{K}}_t - \mathbf{K}_t) \mathbf{H}_t \Sigma_t^f / n \right) + 2 \text{tr} \left((\mathbf{K}_t^\top \mathbb{E}(\hat{\mathbf{K}}_t - \mathbf{K}_t) \mathbf{R}_t / n) \right). \end{aligned} \quad (3.2)$$

The following Theorem 3.1 presents the upper bounds of the discrepancy between the EnKF and the Kalman Filters for the one-step data assimilation.

Theorem 3.1. *Suppose Assumptions 1(i) or 1(ii), 2, 3 hold and the forecast ensemble $\{\mathbf{x}_{t,j}^f\}_{j=1}^n$ are independently sampled from the distribution of $\mathbf{x}_t \mid \mathbf{y}_{1:t-1}$ with mean \mathbf{x}_t^f and covariance Σ_t^f . Then, the forecast and analysis states of the EnKF at time t satisfy*

$$\begin{aligned} p^{-1} \mathbb{E} \| (\hat{\mathbf{x}}_t^f - \mathbf{x}_t^f) \mid \mathbf{y}_{1:t-1} \|^2 &= n^{-1} p^{-1} \text{tr}(\Sigma_t^f) = O(n^{-1}), \\ p^{-1} \mathbb{E} \| (\hat{\mathbf{x}}_t^a - \mathbf{x}_t^a) \mid \mathbf{y}_{1:t} \|^2 &= \text{tr} \left(n^{-1} p^{-1} (\mathbf{I} - \mathbf{K}_t \mathbf{H}_t) \Sigma_t^f \right) + p^{-1} \Omega_t \\ &= O(n^{-1} + p^{-1} \Delta_{\mathbf{K},t} \| \mathbf{y}_t - \mathbf{H}_t \mathbf{x}_t^f \|^2). \end{aligned} \quad (3.3)$$

Theorem 3.1 gives the upper bounds of the one-step data assimilation MSE with high dimensional forecast error covariance estimators, which depends on $\Delta_{\mathbf{K},t}$ whose convergence rates for different covariance estimators are given in (3.1). Specifically, with the banding or mid-banding estimators, the tapering estimator and the thresholding estimator, the

one-step EnKF data assimilation MSE are, respectively,

$$p^{-1}\mathbb{E}\|(\hat{\mathbf{x}}_t^a - \mathbf{x}_t^a)|\mathbf{y}_{1:t}\|^2 \asymp \max\{n^{-1}, p^{-1}q(n^{-1}\log p)^{\alpha/(\alpha+1)}\}, \quad (3.4)$$

$$p^{-1}\mathbb{E}\|(\hat{\mathbf{x}}_t^a - \mathbf{x}_t^a)|\mathbf{y}_{1:t}\|^2 \asymp \max\{n^{-1}, p^{-1}q(n^{-2\alpha/(2\alpha+1)} + n^{-1}\log p)\}, \quad (3.5)$$

$$p^{-1}\mathbb{E}\|(\hat{\mathbf{x}}_t^a - \mathbf{x}_t^a)|\mathbf{y}_{1:t}\|^2 \asymp \max\{n^{-1}, p^{-1}qc_0^2(p)(n^{-1}\log p)^{(1-\gamma)}\}. \quad (3.6)$$

For fixed p, q , both the forecast and analysis states of the EnKF converge to the underlying forecast and analysis states of the Kalman Filter with a convergence rate of \sqrt{n} as $n \rightarrow \infty$ as $\Delta_{\mathbf{K},t} = O(n^{-1})$, as also shown in Theorem S.3.1 of the SM. Furthermore, Proposition S.3.1 implies that with linear model operator \mathcal{M}_t and Gaussian initial state, the asymptotic distributions of $\mathbf{x}_{t,j}^a|\mathbf{y}_{1:t}$ and $\mathbf{x}_{t,j}^f|\mathbf{y}_{1:t-1}$ in the EnKF are the same as those of $\mathbf{x}_t|\mathbf{y}_{1:t}$ and $\mathbf{x}_t|\mathbf{y}_{1:t-1}$ in the Kalman Filter, respectively.

To show the impact of the dimensionality on the MSE, we take the banding and mid-banding estimators as examples. If $q \asymp p$, $p^{-1}\mathbb{E}\|(\hat{\mathbf{x}}_t^a - \mathbf{x}_t^a)|\mathbf{y}_{1:t}\|^2 = O((n^{-1}\log p)^{2\alpha/(2(\alpha+1))})$, which implies that the one-step assimilation MSE mainly depends on the estimation error of the Kalman gain matrix. Commonly in high resolution data assimilation, the dimension of the observation \mathbf{y}_t is much smaller than that of the state vector \mathbf{x}_t , so that $q \ll p$. If q is relatively large such that $p^{-1}q(n^{-1}\log p)^{\alpha/(\alpha+1)} \gg n^{-1}$, then the estimation error of the Kalman gain matrix will dominate, that is, $p^{-1}\mathbb{E}\|(\hat{\mathbf{x}}_t^a - \mathbf{x}_t^a)|\mathbf{y}_{1:t}\|^2 = O(p^{-1}q(n^{-1}\log p)^{\alpha/(\alpha+1)})$. Otherwise, the first term n^{-1} dominates. For the impact of the observation dimension q on the MSE, a study reported in the SM shows that if the additional observation $y_{t,q+1}$ is not far away from its forecast $\mathbf{H}_t\mathbf{x}_t^f$, the MSE will decrease as the first term in (3.3) will decrease as q increases.

For the discrepancies between the EnKF analysis state and the true state, as $\mathbb{E}\|(\hat{\mathbf{x}}_t^a - \mathbf{x}_t)|\mathbf{y}_{1:t}\|^2 = \mathbb{E}\|(\hat{\mathbf{x}}_t^a - \mathbf{x}_t^a)|\mathbf{y}_{1:t}\|^2 + \mathbb{E}\|(\mathbf{x}_t^a - \mathbf{x}_t)|\mathbf{y}_{1:t}\|^2$ and \mathbf{x}_t is a random variable with $\mathbb{E}\|(\mathbf{x}_t^a - \mathbf{x}_t)|\mathbf{y}_{1:t}\|^2 = \text{tr}(\Sigma_t^a)$ which is a constant not related to the ensemble size n for a

fixed p , then $\mathbb{E}\|(\hat{\mathbf{x}}_t^a - \mathbf{x}_t)|\mathbf{y}_{1:t}\|^2$ can not converge to zero.

In practice, the data assimilation process can be repeated for multiple time steps ahead to make longer-time predictions. The following Theorem 3.2 gives the h -step MSE bounds between the forecast/analysis states of the EnKF in comparison to the underlying Kalman Filters. To simplify writing, define two non-stochastic constants

$$C_{t,h}^A = \frac{1 - L_{t,h}^h A_{t,h}^h}{1 - L_{t,h} A_{t,h}} \quad \text{and} \quad C_{t,h}^B = \frac{1 - L_{t,h}^h B_{t,h}^h}{1 - L_{t,h} B_{t,h}}, \quad (3.7)$$

where $A_{t,h} = \max_{t < k \leq t+h} \|\mathbf{I} - \mathbf{K}_k \mathbf{H}_k\|$, $B_{t,h} = \max_{t < k \leq t+h} \{\mathbb{E}\|\mathbf{I} - \hat{\mathbf{K}}_k \mathbf{H}_k\|\}$, and $L_{t,h} = \max_{0 < k \leq h} \{\ell_0, \ell_{t+k}\}$ for a fixed t , with ℓ_0 and ℓ_t defined in Assumption 1. We further denote

$$U_k = \left\{ \|\mathbf{y}_k - \mathbf{H}_k \mathbf{x}_k^f\|^2 \Delta_{\mathbf{K},k} + \text{tr} \left(\mathbb{E}(\hat{\mathbf{K}}_k - \mathbf{K}_k)^T (\hat{\mathbf{K}}_k - \mathbf{K}_k) (\mathbf{H}_k \Sigma_k^f \mathbf{H}_k^T + \mathbf{R}_k) \right) \right\}^{1/2}. \quad (3.8)$$

Theorem 3.2. *Assumptions 1(i) or 1(ii), 2, 3 hold and the analysis ensemble $\{\mathbf{x}_{t,j}^a\}_{j=1}^n$ is generated independently from the distribution of $\mathbf{x}_t | \mathbf{y}_{1:t}$ with mean \mathbf{x}_t^a and covariance Σ_t^a at time t . By repeatedly performing the ensemble forecast-analysis process h steps, the forecast and analysis states of the EnKF at the time $t+h$ satisfy*

$$\begin{aligned} p^{-1} \mathbb{E}\|(\hat{\mathbf{x}}_{t+h}^f - \mathbf{x}_{t+h}^f)|\mathbf{y}_{1:t+h-1}\|^2 &\leq p^{-1} \left(\{\text{tr}(n^{-1} \Sigma_{t+h}^f)\}^{1/2} + L_{t,h} C_{t,h-1}^B \max_{t < k \leq t+h-1} U_k \right)^2 \\ &= O \left(n^{-1} + p^{-1} L_{t,h}^2 (C_{t,h-1}^A)^2 \max_{t < k \leq t+h-1} \{\Delta_{\mathbf{K},k} \|\mathbf{y}_k - \mathbf{H}_k \mathbf{x}_k^f\|^2\} \right), \\ p^{-1} \mathbb{E}\|(\hat{\mathbf{x}}_{t+h}^a - \mathbf{x}_{t+h}^a)|\mathbf{y}_{1:t+h}\|^2 &\leq p^{-1} \left(\{\text{tr}(n^{-1} \Sigma_{t+h}^a)\}^{1/2} + C_{t,h}^B \max_{t < k \leq t+h} U_k \right)^2 \\ &= O \left(n^{-1} + p^{-1} (C_{t,h}^A)^2 \max_{t < k \leq t+h} \{\Delta_{\mathbf{K},k} \|\mathbf{y}_k - \mathbf{H}_k \mathbf{x}_k^f\|^2\} \right). \end{aligned}$$

Compared with the one-step results given in Theorem 3.1, the term related to the estimation error of $\hat{\Sigma}_{t+k}^f$ in the h -step analysis MSE is inflated with constants $(C_{t,h}^A)^2$ which are related to $L_{t,h}$ and $A_{t,h}$ defined before (3.7). However, for any fixed h , $\mathbb{E}\|(\hat{\mathbf{x}}_{t+h}^a - \mathbf{x}_{t+h}^a)|\mathbf{y}_{1:t+h}\|^2 \asymp \mathbb{E}\|(\hat{\mathbf{x}}_t^a - \mathbf{x}_t^a)|\mathbf{y}_{1:t}\|^2$.

Sometimes, the assimilation process proceeds every k time steps not every step as one may not have observations at each step or the assimilation in every step is too computationally consuming. Theorem S.3.2 of the SM gives the MSE bounds for multiple-step forecasting and assimilation where the assimilation process proceeds every k time steps.

4 Imperfect Models

In practice, the exact form of the model operator \mathcal{M}_t is likely unknown, and the state-of-the-art model $\hat{\mathcal{M}}_t$ is only an approximation to \mathcal{M}_t . Besides, large dynamic models in earth science are often nonlinear, one may use its linear approximation (Julier and Uhlmann, 1997; Stroud et al., 2010). This section is devoted to quantifying the effects of the model approximation error on the accuracy of the analysis and forecast states of the EnKF. The following assumption regulates the extent of the model approximation error.

Assumption 4. Let $\xi_t = \hat{\mathcal{M}}_t(\mathbf{x}) - \mathcal{M}_t(\mathbf{x})$ be the error of the approximated model $\hat{\mathcal{M}}_t$ to \mathcal{M}_t with $\mathbb{E}(\xi_t) = \mu_{\xi_t}$ and $\text{Var}(\xi_t) = \Xi_{\xi_t}$. It is assumed that $\|\mu_{\xi_t}\|_{\infty} \leq C_1$ and $\|\Xi_{\xi_t}\| \leq C_2$ for some positive constants C_1 and C_2 .

Theorem 4.1 presents the one-step assimilation bounds of the difference between the forecast/analysis states of the EnKF and the Kalman Filter when \mathcal{M}_t is unknown. Denote

$$\begin{aligned}
V_t &= \text{tr} \left(n^{-1} (\mathbf{I} - \mathbf{K}_t \mathbf{H}_t)^T (\mathbf{I} - \mathbf{K}_t \mathbf{H}_t) \Xi_{\xi_t} \right) + \| (\mathbf{I} - \mathbf{K}_t \mathbf{H}_t) \mu_{\xi_t} \|^2 \\
&+ \text{tr} \left(n^{-1} \mathbb{E}(\hat{\mathbf{K}}_t - \mathbf{K}_t)^T (\hat{\mathbf{K}}_t - \mathbf{K}_t) (\mathbf{H}_t (\boldsymbol{\Sigma}_t^f + \Xi_{\xi_t}) \mathbf{H}_t^T + \mathbf{R}_t) \right) \\
&+ \mathbb{E} \| (\hat{\mathbf{K}}_t - \mathbf{K}_t) (\mathbf{y}_t - \mathbf{H}_t \mathbf{x}_t^f - \mathbf{H}_t \mu_{\xi_t}) \|^2 + 2 \text{tr} \left(\mathbf{K}_t^T \mathbb{E}(\hat{\mathbf{K}}_t - \mathbf{K}_t) \mathbf{R}_t / n \right) \\
&- 2 \text{tr} \left((\mathbf{I} - \mathbf{K}_t \mathbf{H}_t)^T \mathbb{E}(\hat{\mathbf{K}}_t - \mathbf{K}_t) \left\{ \mathbf{H}_t (\boldsymbol{\Sigma}_t^f + \Xi_{\xi_t}) / n + (\mathbf{y}_t - \mathbf{H}_t \mathbf{x}_t^f - \mathbf{H}_t \mu_{\xi_t}) \mu_{\xi_t}^T \right\} \right).
\end{aligned} \tag{4.1}$$

Theorem 4.1. *Suppose Assumptions 1(i) or 1(ii), 2, 3, 4 hold and $\{\mathbf{x}_{t-1,j}^a\}_{j=1}^n$ is generated independently from the distribution of $\mathbf{x}_{t-1} \mid \mathbf{y}_{1:t-1}$ with mean \mathbf{x}_{t-1}^a and covariance $\boldsymbol{\Sigma}_{t-1}^a$ at*

time $t - 1$. Then, the forecast and analysis states of the EnKF satisfy

$$p^{-1}\mathbb{E}\|(\hat{\mathbf{x}}_t^f - \mathbf{x}_t^f)|\mathbf{y}_{1:t-1}\|^2 = n^{-1}p^{-1}\text{tr}(\boldsymbol{\Sigma}_t^f + \boldsymbol{\Xi}_{\xi_t}) + p^{-1}\|\mu_{\xi_t}\|^2, \quad (4.2)$$

$$\begin{aligned} p^{-1}\mathbb{E}\|(\hat{\mathbf{x}}_t^a - \mathbf{x}_t^a)|\mathbf{y}_{1:t}\|^2 &= p^{-1}\text{tr}\left(n^{-1}(\mathbf{I} - \mathbf{K}_t\mathbf{H}_t)\boldsymbol{\Sigma}_t^f\right) + V_t \\ &= O\left(n^{-1} + p^{-1}\|(\mathbf{I} - \mathbf{K}_t\mathbf{H}_t)\mu_{\xi_t}\|^2 + p^{-1}\|\mathbf{y}_t - \mathbf{H}_t\mathbf{x}_t^f\|^2(\|\boldsymbol{\Xi}_{\xi_t}\|^2 + \tilde{\Delta}_{\mathbf{K},t})\right) \end{aligned} \quad (4.3)$$

where $\tilde{\Delta}_{\mathbf{K},t} = \mathbb{E}\|\tilde{\mathbf{K}}_t - \mathbf{K}_t\|^2$ and $\tilde{\mathbf{K}}_t$ is the estimate of \mathbf{K}_t with true model \mathcal{M}_t .

The theorem suggests that the model approximation error creates extra terms related to μ_{ξ_t} and $\|\boldsymbol{\Xi}_{\xi_t}\|$, which are absent from the results in Theorem 3.1 where accurate model is assumed. Specifically, the assimilation MSEs for fixed p, q and $p, q \rightarrow \infty$ are, respectively,

$$\mathbb{E}\|(\hat{\mathbf{x}}_t^a - \mathbf{x}_t^a)|\mathbf{y}_{1:t}\|^2 \asymp \max\{n^{-1}, \|(\mathbf{I} - \mathbf{K}_t\mathbf{H}_t)\mu_{\xi_t}\|^2, \|\boldsymbol{\Xi}_{\xi_t}\|^2\} \text{ and} \quad (4.4)$$

$$p^{-1}\mathbb{E}\|(\hat{\mathbf{x}}_t^a - \mathbf{x}_t^a)|\mathbf{y}_{1:t}\|^2 \asymp \max\{n^{-1}, p^{-1}\|(\mathbf{I} - \mathbf{K}_t\mathbf{H}_t)\mu_{\xi_t}\|^2, p^{-1}q\tilde{\Delta}_{\mathbf{K},t}, p^{-1}q\|\boldsymbol{\Xi}_{\xi_t}\|^2\}.$$

If $\|\boldsymbol{\Xi}_{\xi_t}\| \neq 0$ but $\mu_{\xi_t} = \mathbf{0}$, which means $\hat{\mathcal{M}}_t$ is unbiased to \mathcal{M}_t , then for fixed p and q , $\mathbb{E}\|(\hat{\mathbf{x}}_t^a - \mathbf{x}_t^a)|\mathbf{y}_{1:t}\|^2 = O(n^{-1} + \|\boldsymbol{\Xi}_{\xi_t}\|^2)$. Thus, if $\|\boldsymbol{\Xi}_{\xi_t}\|^2 = O(n^{-1})$, then $\mathbb{E}\|(\hat{\mathbf{x}}_t^a - \mathbf{x}_t^a)|\mathbf{y}_{1:t}\|^2 = O(n^{-1})$, that is, the model approximation error does not alter the order of magnitude of the assimilation MSEs of the EnKF. However, if $n\|\boldsymbol{\Xi}_{\xi_t}\|^2 \rightarrow \infty$, then $\mathbb{E}\|(\hat{\mathbf{x}}_t^a - \mathbf{x}_t^a)|\mathbf{y}_{1:t}\|^2 = O(\|\boldsymbol{\Xi}_{\xi_t}\|^2)$, which means the model approximation error dominates the assimilation MSE. When $p, q \rightarrow \infty$, $p^{-1}\mathbb{E}\|(\hat{\mathbf{x}}_t^a - \mathbf{x}_t^a)|\mathbf{y}_{1:t}\|^2 \asymp \max\{n^{-1}, p^{-1}q\tilde{\Delta}_{\mathbf{K},t}, p^{-1}q\|\boldsymbol{\Xi}_{\xi_t}\|^2\}$.

The above analysis shows that for both the fixed and diverging dimensions and both the unbiased and biased approximation of \mathcal{M}_t , the approximation errors as represented by μ_{ξ_t} and $\|\boldsymbol{\Xi}_{\xi_t}\|^2$ contributes substantially to the assimilation MSE, which suggests that a good approximation of the model operator is a significant aspect of data assimilation. While this may be obvious, Theorem 4.1 describes exactly how it happens. The accumulation of the model approximation error is more pronounced in the h -step assimilation MSEs as shown in Theorem S.3.3 of the SM. Thus, an iterative HD-EnKF algorithm is introduced in

S.1.2 to account for the model approximation error to some extent since most geophysical models are imperfect in practice, of which the main idea is to substitute $\hat{\mathbf{x}}_t^f$ in the original forecast sample covariance matrix by the analysis state $\hat{\mathbf{x}}_t^a$ in the iteration.

5 Simulation

This section reports results of simulation studies performed on two popular geophysical models, the Lorenz-96 and the Shallow Water Equation models, to demonstrate the proposed HD-EnKF algorithms. These two models are often used for testing new approaches in atmospheric sciences for both data assimilation and the spatial-temporal forecasts. The proposed HD-EnKF methods are compared with the standard EnKF and the inflation method (Liang et al., 2012) under both the correct and imperfect models. Details of the proposed HD-EnKF algorithms are given in Section S.1 of the SM, including the consistent HD-EnKF update in S.1.1 and the iterative HD-EnKF update algorithms in S.1.2, which are based on the consistent estimators of the forecast error covariance matrix Σ_t^f by the banding, mid-banding, tapering and thresholding estimators.

5.1 Lorenz-96 model

Lorenz-96 model (L96; Lorenz, 1996) is a continuous in time but discrete in space model for modeling spatially extended chaotic systems in the atmosphere. It is a nonlinear model for continuous evolution of atmospheric variables such as temperature or vorticity at p locations on a latitude circle defined by the ordinary differential equation

$$d\mathbf{x}_t^{(j)}/dt = (\mathbf{x}_t^{(j+1)} - \mathbf{x}_t^{(j-2)})\mathbf{x}_t^{(j-1)} - \mathbf{x}_t^{(j)} + F \triangleq f_j(\mathbf{x}_t, t), \text{ for } j = 1, \dots, p, \quad (5.1)$$

with $\mathbf{x}_t^{(-1)} = \mathbf{x}_t^{(p-1)}$, $\mathbf{x}_t^{(0)} = \mathbf{x}_t^{(p)}$ and $\mathbf{x}_t^{(p+1)} = \mathbf{x}_t^{(1)}$, where $\mathbf{x}_t^{(j)}$ denotes the j^{th} dimension of the state variable \mathbf{x}_t , $(\mathbf{x}_t^{(j+1)} - \mathbf{x}_t^{(j-2)})\mathbf{x}_t^{(j-1)}$ is the nonlinear term, $-\mathbf{x}_t^{(j)}$ is the damping term and F is a forcing term.

L96 can be solved approximately via the fourth-order Runge-Kutta time integration scheme (RK4; Butcher, 2016). An approximation to the true state was simulated by (i) implementing the RK4 method with a finer time step, say $h = 0.05$; and (ii) adding a random noise at each time step so that $\mathbf{x}_{t+1} = \mathcal{M}_{t+1}(\mathbf{x}_t) + \mathbf{w}_{t+1}$. In our experiment, $\mathbf{w}_t \sim \mathcal{N}(0, \sigma_0 \mathbf{I}_p)$ and σ_0 were set as 0.1, 0.25 and 0.5, respectively.

We experimented $p = 40$ and 100 , under which the system behaves chaotically, since the L96 model behaves like chaos for $p \geq 7$ (Bedrossian et al., 2022). The true forcing was $F = 8$. We also considered the misspecified model setting by making $F = 6, 7, 9, 10$ in the assimilation processes, corresponding to the imperfect models in Section 4. The initial state was $x_1^{(j)} = F$ for $j \neq 20$ and $x_1^{(20)} = F + 0.001$, and the initial forecast ensemble was generated by $\mathbf{x}_{1,j}^f = \mathbf{x}_1 + \mathcal{N}_p(0, 0.1\mathbf{I}_p)$ for $j = 1, \dots, n$.

The observations \mathbf{y}_t were made at q randomly selected components of the state vector \mathbf{x}_t with $q = 30, 40$ and 100 while $p = 40$ and 100 , respectively, followed by adding observation errors $\boldsymbol{\varepsilon}_t \stackrel{IID}{\sim} \mathcal{N}_q(0, \mathbf{R}_t)$ to the true states. The (i, j) -element of \mathbf{R}_t was $R_{ij} = 0.5^{\min\{|i-j|, q-|i-j|\}}$, which prescribes spatially correlated observation errors. The observation operator \mathbf{H}_t was a $q \times p$ matrix with the (j, i) element being 1 if and only if the j -th component of \mathbf{y}_t was the observed i -th dimension of the state \mathbf{x}_t . We simulated observations every 4 time steps for a total of 2000 steps and reported the results for the last 1000 steps to allow the system to settle down. The ensemble size n was 20, 30, 60 and 90. All the experiments were repeated 500 times.

We considered the HD-EnKF schemes using the banding, mid-banding, tapering and

thresholding covariance estimators, which were compared with the standard EnKF that utilizes the sample covariance to estimate the forecast error covariance and the inflation methods (Liang et al., 2012). The performances of these methods were evaluated by the root-mean-square error (RMSE) of the analysis state $\hat{\mathbf{x}}_t^a$ to (i) the underlying analysis state \mathbf{x}_t^a by the Kalman Filter utilizing the true covariances and (ii) the true state \mathbf{x}_t . To gain accurate estimations of Σ_t^f for the oracle analysis \mathbf{x}_t^a , we used the standard EnKF with a very large ensemble size 1000 (relative to p in the simulation), and used the sample covariance matrices to replace Σ_t^f in the Kalman filter update formula to obtain \mathbf{x}_t^a .

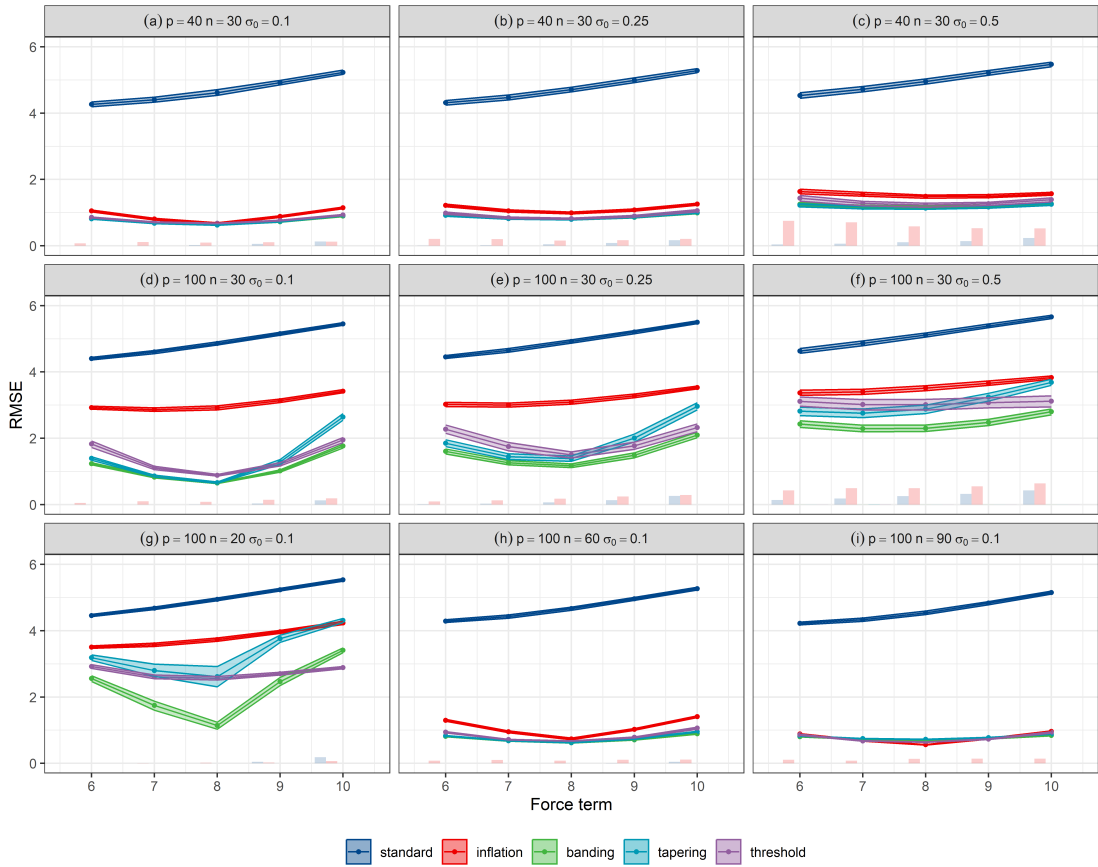


Figure 2: Average RMSEs to the oracle analysis state and their 25 – 75% quantile bands (color bands) as a function of forcing F used in \mathcal{M}_t (true value is 8) by the standard EnKF (blue), the modified EnKF methods: the inflation (red), banding (green), tapering (cyan) and thresholding (purple) for $p = q = 40$ and 100, $n = 20, 30, 60, 90$, $\sigma_0 = 0.1, 0.25$ and 0.5, respectively. The light-colored bars in the lower part of each panel denote the divergence rates of the assimilation schemes.

Figure 2 displays the average RMSEs to the oracle analysis state of the five assimila-

tion methods, namely the standard EnKF, the inflation method and the three HD-EnKFs equipped with the banding and tapering (both respect the circular bandable structures), and the thresholding estimators, under different forcing F at moderate dimension $p = 40$ and high dimension $p = 100$ with different σ_0 and n . It shows that the HD-EnKF with the three high dimensional covariance estimators had much smaller RMSEs than the standard EnKF and the inflation methods at both the correct ($F = 8$) and misspecified ($F \neq 8$) models. Even when F deviated more from the true value 8, the HD-EnKFs still achieved analysis states that were much closer to the oracle than the inflation method although both strains of methods showed increased RMSEs with respect to $|F - 8|$. The standard EnKF with the sample covariance estimator to Σ_t^f had much larger assimilation errors in all cases.

Comparing Figure 2's panels (d)-(f) with panels (a)-(c), the advantages of the proposed HD-EnKFs over the inflation method were more apparent for the higher dimension $p = 100$. The analysis RMSEs of the HD-EnKFs kept at a lower level especially when the force F was equal or close to the true value ($F = 8$), while the analysis RMSE of the inflation method ranked behind but better than the standard EnKF. This means that the HD-EnKFs are quite attractive as the geophysical models in earth science are of ultra high dimension. The figure also displays the percentages of divergence of the five methods. It shows that the inflation method endured quite high divergences which increased substantially with the model error (e.g. reached 50% when $\sigma = 0.5$), even higher than the standard EnKF. In contrast, the three HD-EnKF methods had quite low divergence rates for all cases.

Panels (d), (g)-(f) of Figure 2 demonstrate the influence of the ensemble size on the analysis RMSEs. Although the analysis RMSEs of the inflation and the HD-EnKF methods all became smaller with the increase of the ensemble size n , the proposed HD-EnKFs outperformed the inflation method, especially when the ensemble size n was small (panels

(d) and (g) with $n = 20$). This suggests that the proposed methods could provide more accurate analysis states when the ensemble size was not big enough. Ensemble size is a significant restriction for the large geophysical models as they are extremely costly to run.

Table 1: Average RMSEs to the oracle analysis state and true state of the five EnKF schemes and their divergence rates (in parentheses) for Lorenz-96 model with $p = 40$, $q = 30$, $n = 30$, $\sigma_0 = 0.1$, and $F = 8$ for the correct and other F values for misspecified models.

	method	F=6	F=7	F=8	F=9	F=10
oracle	standard	4.26 (0.01)	4.43 (0.06)	4.69 (0.15)	5.05 (0.29)	5.41 (0.54)
	inflation	1.32 (0.80)	0.96 (0.65)	0.77 (0.63)	1.03 (0.69)	1.38 (0.86)
	banding	1.10 (0.11)	0.90 (0.08)	0.83 (0.09)	0.99 (0.12)	1.27 (0.29)
	tapering	1.08 (0.13)	0.87 (0.07)	0.79 (0.06)	0.99 (0.13)	1.31 (0.25)
	threshold	1.12 (0.06)	0.90 (0.02)	0.84 (0.04)	1.00 (0.04)	1.35 (0.16)
true	standard	4.28 (0.01)	4.44 (0.06)	4.70 (0.15)	5.05 (0.29)	5.40 (0.54)
	inflation	1.42 (0.80)	1.04 (0.65)	0.84 (0.63)	1.11 (0.69)	1.47 (0.86)
	banding	1.23 (0.11)	1.01 (0.08)	0.93 (0.09)	1.09 (0.12)	1.37 (0.29)
	tapering	1.21 (0.13)	0.98 (0.07)	0.90 (0.06)	1.09 (0.13)	1.42 (0.25)
	threshold	1.24 (0.06)	1.00 (0.02)	0.93 (0.04)	1.09 (0.04)	1.44 (0.16)

Table 1 displays the analysis RMSEs of different methods and their divergence rates under sparser observations $q = 30$ while $p = 40$, which illustrates the influence of the sparsity in the observations on the assimilation accuracy. Although the analysis RMSEs of different assimilation methods were slightly higher than those under more observations $p = q = 40$, the RMSEs of the HD-EnKF methods were smaller than those of the other methods for imperfect models ($F \neq 8$) and were comparable to the inflation method for the correct model ($F = 8$). However, it is noted that the inflation method had a higher divergence rate which reached 63% even under the correct model ($F = 8$) while the proposed methods had low divergence rates, showing their robustness to the sparsity of the observations.

5.2 Shallow Water Equation model

The second experiment was conducted on the Shallow Water Equation model (SWE). The SWE is a system of hyperbolic/parabolic partial differential equations governing fluid flow, which is widely used in river flow simulations, as well as in other settings where the water depth is significantly lower than the horizontal length scale of motion. The barotropic nonlinear SWE takes the following form (Lei et al., 2012), for $0 \leq z_1 \leq L, 0 \leq z_2 \leq D$,

$$\begin{aligned} \frac{\partial u}{\partial t} + u \frac{\partial u}{\partial z_1} + v \frac{\partial u}{\partial z_2} - f v &= -g \frac{\partial h}{\partial z_1} + k \nabla^2 u, \\ \frac{\partial v}{\partial t} + u \frac{\partial v}{\partial z_1} + v \frac{\partial v}{\partial z_2} + f u &= -g \frac{\partial h}{\partial z_2} + k \nabla^2 v, \\ \frac{\partial h}{\partial t} + u \frac{\partial h}{\partial z_1} + v \frac{\partial h}{\partial z_2} &= -h \left(\frac{\partial u}{\partial z_1} + \frac{\partial v}{\partial z_2} \right) + k \nabla^2 h, \end{aligned} \quad (5.2)$$

where the fluid velocity components u in z_1 direction and v in z_2 direction as well as the fluid depth h are the model variables, g is the gravity acceleration 9.8 m s^{-2} , f is the Coriolis parameter defined as constant 10^{-4} s^{-1} , k is the diffusion coefficient specified as $5 \times 10^4 \text{ m}^2 \text{ s}^{-1}$, and L and D are the domain limits set as 500 km and 300 km, respectively. The SWE was discretized with a uniform grid spacing of 10 km in the z_1 and z_2 directions and solved by the Lax-Wendroff method with a time step of 30 seconds. Thus, the SWE model had a dimension of $p' = 50 \times 31$ for each state variable u, v, h , leading to the state vector $\mathbf{x}_t = (u_t, v_t, h_t)^T$ of dimension $p = 3p' = 4650$. The initial height (depth) field was given by $h(z_1, z_2) = H_0 + H_1 \tanh(9(D/2 - z_2)/2/D) + H_2 \text{sech}^2(9(D/2 - z_2)/D) \sin(2\pi z_1/L)$, where H_0, H_1 and H_2 were set to be 50 m, 5.5 m and 3.325 m, respectively. The initial velocity field was derived from the initial height field with the geostrophic relation.

The SWE was simulated for 48 hours with a total of 5760 time steps at 30 second intervals after a half hour (60-steps) pre-running. The observations of u, v and h were made at $q' = 310$ grid points from 10 randomly selected rows in each direction every 3 hours, making the whole observation vector $\mathbf{y}_t = (u_t, v_t, h_t)^T$ be of dimension $q = 3q' = 930$, which

means the observations were quite sparse with $q = 0.2p$. To generate the imperfect models, the diffusion coefficient k was also considered as $10^4 \text{ m}^2 \text{ s}^{-1}$ in the assimilation process. The observation error variances were $\sigma_u^2 = \sigma_v^2 = 0.5, \sigma_h^2 = 1.0$ for the three dimensions and $\mathbf{R}_t = \text{diag}(\sigma_u^2 \mathbf{I}_{p'}, \sigma_v^2 \mathbf{I}_{p'}, \sigma_h^2 \mathbf{I}_{p'})$. The ensemble size n was 100, and the initial ensemble was generated by adding random noises from $N_p(0, \mathbf{I}_p)$ to the initial state \mathbf{x}_1 .

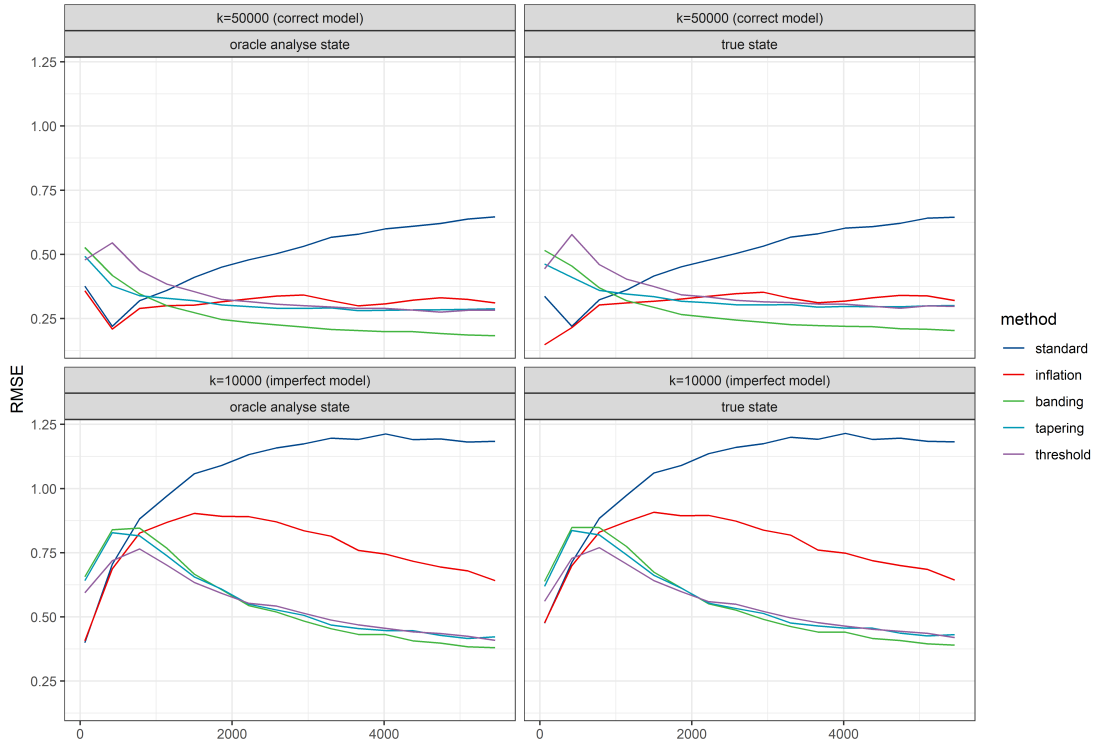


Figure 3: RMSEs to the oracle analysis state (the left panels) and the true state (the right panels) at each assimilation time step by the standard, inflation, banding, tapering and threshold under the correct model ($k = 5 \times 10^4$) and imperfect model ($k = 10^4$) with $n = 100$, $p = 4650$ and $q = 930$ on the SWE model.

Figure 3 reports the RMSEs at each assimilation time step of the five EnKF methods (the standard EnKF, inflation and three HD-EnKF) to the oracle analysis states \mathbf{x}_t^a and the true states \mathbf{x}_t under the correct ($k = 5 \times 10^4$) and the imperfect ($k = 10^4$) models while Table 2 summarizes the average analysis RMSEs over the last 24 hours (2880 steps), together with their 25% and 75% quantiles. Figure 3 shows the three proposed HD-EnKF methods outperformed the inflation and the standard EnKF methods for both the correct

Table 2: Average RMSEs to the oracle analysis state and true state over the last 24 hours (2880 steps) of the simulation experiments and their 25% and 75% quantiles (in parentheses) by the five EnKF schemes for the SWE model under the correct ($k = 5 \times 10^4$) and the imperfect ($k = 10^4$) models with $n = 100$, and $p = 4650$ and $q = 930$.

method	k = 50000 (correct model)		k = 10000 (imperfect model)	
	oracle	true	oracle	true
standard	0.61 (0.45, 0.76)	0.62 (0.47, 0.78)	1.16 (1.05, 1.26)	1.18 (1.07, 1.28)
inflation	0.34 (0.27, 0.40)	0.38 (0.31, 0.44)	0.75 (0.68, 0.82)	0.77 (0.70, 0.84)
banding	0.20 (0.17, 0.22)	0.26 (0.23, 0.28)	0.42 (0.40, 0.45)	0.46 (0.43, 0.48)
tapering	0.25 (0.23, 0.28)	0.30 (0.28, 0.33)	0.44 (0.41, 0.46)	0.47 (0.44, 0.50)
threshold	0.28 (0.26, 0.30)	0.33 (0.31, 0.35)	0.44 (0.42, 0.46)	0.48 (0.46, 0.50)

and imperfect models with much smaller RMSEs after the system settled down and that the superiority became more apparent over time, especially under the misspecified model. Specifically, the RMSEs at each assimilation time step of the three proposed HD-EnKF schemes became lower and lower over time compared to increased RMSEs for the standard EnKF for all cases and slight increases RMSEs for the inflation method under true models.

It is obvious from Table 2 that the HD-EnKF methods had significantly lower RMSEs and narrower 25%-75% quantile bands with more evident superiority under imperfect models. Specifically, the proposed HD-EnKFs were able to reduce the RMSE by 41% compared to the inflation method, implying that the proposed methods could attain more accurate and robust assimilated outcomes even under extremely sparse observations and ultra-high dimensional state variables. Thus, the proposed methods are highly appealing, especially considering that geophysical models in earth science often possess ultra-high dimensions.

6 Sea Temperature Assimilation in Northwest Pacific

This section demonstrates how the proposed method is applied to sea temperature assimilation based on the oceanography model named Regional Oceanic Modeling System (ROMS) with satellite data. ROMS is a three-dimensional, free-surface, terrain-following ocean general circulation model that solves the Reynolds-averaged Navier–Stokes equations using the hydrostatic and Boussinesq assumptions (Shechetkin and McWilliams, 2005; Haidvogel et al., 2008). While the satellites produce high-resolution sea surface temperature data, they can not provide ocean measurement beneath the ocean surface where the physical model ROMS plays a key role.

The data assimilation was conducted from January 1st, 2008 to March 31st, 2008 over a study area 25.5N-34.7N, 144.4E-154E. The spatial resolution of the ROMS was $0.56^\circ \times 0.49^\circ$ with 18×20 horizontal grids and 18 uneven vertical layers over the water column, making the dimension p for the state variable of sea temperature (\mathbf{x}_t) to be $6480 = 18 \times 20 \times 18$. To scale down the computation, we did not include the other ocean variables namely salinity and current velocity as the assimilated variables, and let them be internally determined by ROMS at each step with the sea temperature as the assimilated variables. The assimilation time length was daily which was also the frequency of the observations. The satellite data were the daily Optimum Interpolation Sea Surface Temperature (OISST; <https://www.ncei.noaa.gov/products>). OISST is a long-term data records for Sea Surface Temperature (SST) that incorporate satellite observations into regular global grids using ships and buoys observations correct satellite SST biases (Banzon and Reynolds, 2013). As the OISST only provides sea surface temperature, the observation dimension was $q = 360$.

To run ROMS, we need to input the initial state of sea temperature \mathbf{x}_1 , the boundary conditions and smoothed bathymetry data (sea bottom topography). The bathymetry data

came from ETOPO2 (<https://www.ncei.noaa.gov/products/etopo-global-relief-model>), which is a global map of the earth’s seafloor and land elevations as shown in Figure S.1 of the SM. The initial state (\mathbf{x}_1) was from the Global Ocean Reanalysis and Simulations (GLORYS; <https://data.marine.copernicus.eu/products>) on January 1st. Thorough descriptions of boundary conditions of ROMS can be found in [Marchesiello et al. \(2001\)](#).

As the ocean temperature, salinity and current fields have different spatial scales and resolution in the three dimension study region both in the ROMS and the physical ocean, we transform the study region to a scale down space to facilitate the bandwidth selection in the banding estimator. Specifically, the grid points in the study region are denoted by coordinates $\{(u, v, h), u = 1, \dots, 18, v = 1, \dots, 20, h = 1, \dots, 18\}$ in the transformed space of unit rectangles, where the banding estimator is performed. The temperatures on the physical grids are labelled as $\{x_{u,v,h}\}$ in the standardized grids and the whole state vector can be labelled by $\mathbf{x} = (x_{1,1,1}, \dots, x_{18,20,18})^T$ with the subscript t hidden. The banding estimator with bandwidth k means that we keep the covariances between $x_{u,v,h}$ and $x_{u',v',h'}$ on the standardized grids if they satisfy $\max\{|u' - u|, |v' - v|, |h' - h|\} \leq k$.

We performed the HD-EnKF using the banding estimator with an ensemble size of $n = 30$ to obtain the assimilated three-dimensional sea temperature for the study period and region. We also compared the proposed method with the standard EnKF and the inflation method. The out-of-sample performances of these methods were assessed on data collected under the ocean Argo project over the study period and region, accessed at <https://argo.ucsd.edu/data/>. The Argo project collects information from inside the ocean using floats that initially drift with the ocean currents and then surface up and down between the surface and mid-sea to collect measurements. As the observations provided by Argo are in-situ observations at various depths, they are more precise than the remote

sensing data by the satellites, and hence, are used as substitutes for the ground truth for the out-of-sample assessment. The bandwidth k used in the banding estimator was $k = 1$, selected by minimizing the out-of-sample RMSE over the first month of the study period between assimilated temperatures and temperatures recorded by Argo at different depths. The inflation factor for the inflation method was similarly selected, which was 1.1.

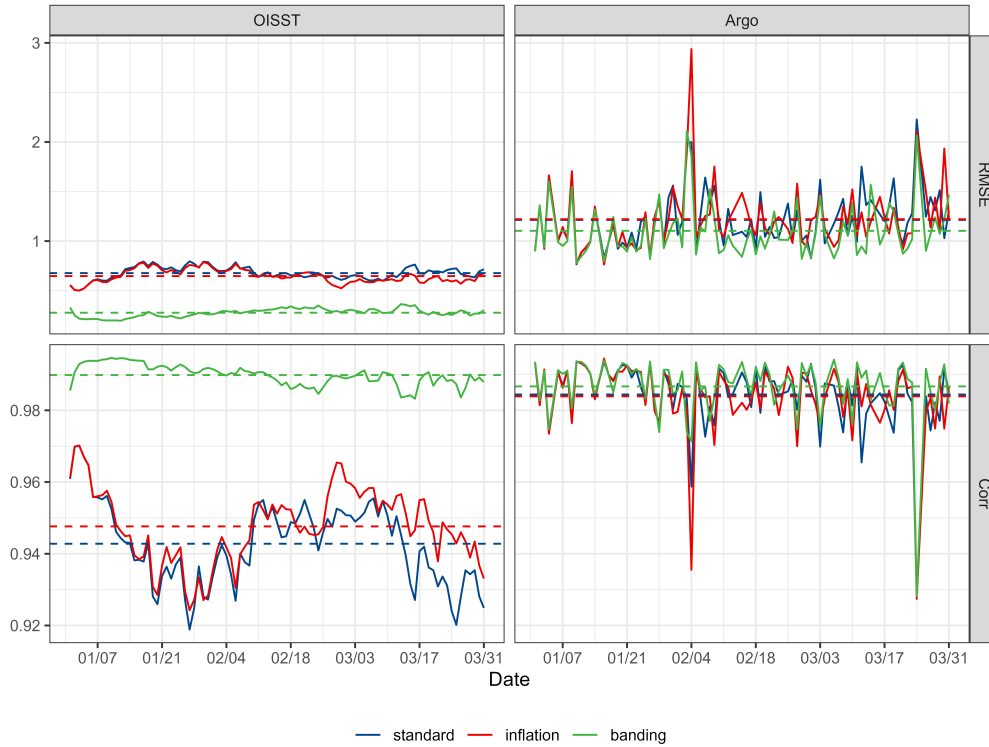


Figure 4: Daily assimilation RMSEs and correlations to the OISST(left panels) and the Argo data (right panels) from Jan. 1st 2008 to Mar. 31st 2008 using the standard EnKF (blue), inflation (red) and HD-EnKF with banding (green), respectively. The dashed horizontal line represents the average assimilation RMSEs and correlations over the whole assimilation period.

Figure 4 displays both the in-sample RMSEs and correlations between the assimilated sea surface temperature and the OISST observations, and the out-of-sample RMSEs and correlation between the assimilated sea water temperature and the temperatures recorded by Argos at various depths. From Figure 4, the HD-EnKF provided much lower and more stable assimilation RMSEs and much higher correlations in the entire assimilation period than those for the standard EnKF and the inflation methods. On the out-of-sample per-

Table 3: The average assimilation RMSEs and correlations and their standard errors (in the parentheses) to the OISST data and the Argo data over the whole assimilation period.

Method	OISST		Argo	
	RMSE	Corr	RMSE	Corr
standard	0.677(0.0067)	0.943(0.0012)	1.242(0.0421)	0.984(0.0013)
inflation	0.647(0.0071)	0.948(0.0011)	1.244(0.0421)	0.983(0.0012)
banding	0.277(0.0043)	0.990(0.0003)	1.134(0.0425)	0.986(0.0014)

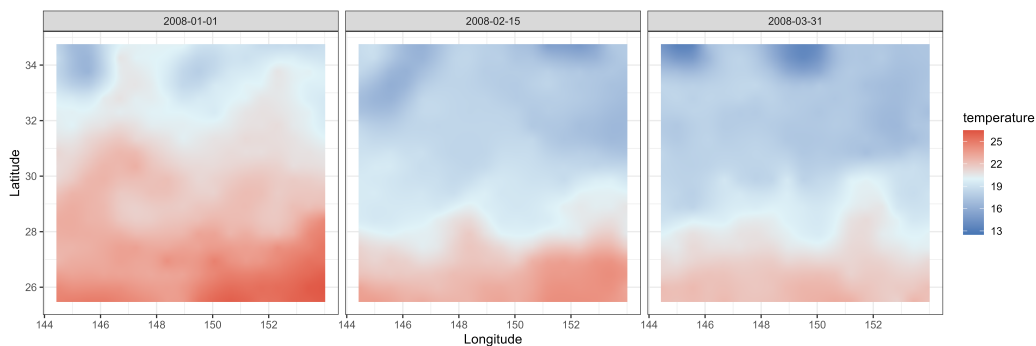


Figure 5: The spatial distribution of the assimilated sea surface temperature on January 1st, February 15th and March 31st in 2008 over the study area, with the fill color from red to blue representing sea surface temperature from high to low.

formance on the Argo data, the HD-EnKF produced assimilated sea temperatures with smaller RMSEs and higher correlations both on average and for most days during the assimilation period. These imply that the proposed HD-EnKF algorithm could offer more accurate and robust assimilation results in practice. Detailed numerical results of these methods are reported in Table 3, which summarizes the average assimilation RMSEs and correlations of the assimilated $\hat{\mathbf{x}}_t^a$ to the OISST and the Argo data over the whole assimilation period. The spatial distribution of the assimilated sea surface temperature over the study area on January 1st, February 15th and March 31st in 2008 is depicted in Figure 5, which varied over time and saw an overall downward trend during the study period.

7 Discussion

In this paper, we propose HD-EnKF algorithms to suit the needs of high dimensional data assimilation. We take the opportunity to study the theoretical properties of the EnKF under both the fixed and the high dimensional cases for both the correct and misspecified models. The study shows that the proposed HD-EnKF can replace the widely used inflation method for data assimilation of a large dynamic system based on two considerations. One is that the established theoretical analysis on the consistency and the error bounds makes the proposed HD-EnKF methods more understandable with a theoretical guarantee; and the other is the better algorithm convergence and smaller RMSEs than the inflation method as shown in the simulation studies and the empirical study on sea temperature assimilation. The latter means that a smaller ensemble size for the EnKF can be used at a given level of accuracy which is particularly attractive as the running of the geophysical models is generally very expensive. The proposed HD-EnKF has great potential for applications in earth science where the geophysical models, the state variables or the observations are ultra-high dimensional, such as global carbon calculation, ocean data assimilation, weather forecasting, sea ice prediction and the generation of high-resolution data sets.

SUPPLEMENTARY MATERIAL

We provide detailed steps of the proposed HD-EnKF algorithm, bandwidth selection of the mid-banding estimator, additional theoretical results and simulation results, and the details for the proofs of the theoretical results in the Supplementary.

References

- Anderson, J. L. and S. L. Anderson (1999). A Monte Carlo implementation of the nonlinear filtering problem to produce ensemble assimilations and forecasts. Monthly Weather Review 127(12), 2741–2758.
- Bai, Z. D. and Y. Q. Yin (1993). Limit of the smallest eigenvalue of a large dimensional sample covariance matrix. The Annals of Probability 21(3), 1275 – 1294.
- Banzon, V. F. and R. W. Reynolds (2013). Use of windsat to extend a microwave-based daily optimum interpolation sea surface temperature time series. Journal of Climate 26(8), 2557 – 2562.
- Bedrossian, J., A. Blumenthal, and S. Punshon-Smith (2022). A regularity method for lower bounds on the Lyapunov exponent for stochastic differential equations. Inventiones mathematicae 227(2), 429–516.
- Bickel, P. J. and E. Levina (2008a). Covariance regularization by thresholding. The Annals of Statistics 36(6), 2577–2604.
- Bickel, P. J. and E. Levina (2008b). Regularized estimation of large covariance matrices. The Annals of Statistics 36(1), 199–227.
- Bouttier, F. and P. Courtier (1999). Data assimilation concepts and methods march 1999.
- Butcher, J. C. (2016). Numerical Methods for Ordinary Differential Equations (First ed.). Wiley.
- Cai, T. T., C.-H. Zhang, and H. H. Zhou (2010). Optimal rates of convergence for covariance matrix estimation. The Annals of Statistics 38(4), 2118–2144.

- Constantinescu, E. M., A. Sandu, T. Chai, and G. R. Carmichael (2007). Ensemble-based chemical data assimilation. I: General approach. Quarterly Journal of the Royal Meteorological Society 133(626), 1229–1243.
- Courtier, P., E. Andersson, W. Heckley, D. Vasiljevic, M. Hamrud, A. Hollingsworth, F. Rabier, M. Fisher, and J. Pailleux (1998). The ECMWF implementation of three-dimensional variational assimilation (3D-Var). I: Formulation. Quarterly Journal of the Royal Meteorological Society 124(550), 1783–1807.
- Evensen, G. (1994). Sequential data assimilation with a nonlinear quasi-geostrophic model using Monte Carlo methods to forecast error statistics. Journal of Geophysical Research 99(C5), 10143.
- Evensen, G., F. C. Vossepoel, and P. J. van Leeuwen (2022). Data Assimilation Fundamentals: A Unified Formulation of the State and Parameter Estimation Problem. Cham: Springer International Publishing.
- Furrer, R. and T. Bengtsson (2007). Estimation of high-dimensional prior and posterior covariance matrices in Kalman filter variants. Journal of Multivariate Analysis 98(2), 227–255.
- Furrer, R., M. G. Genton, and D. Nychka (2006). Covariance tapering for interpolation of large spatial datasets. Journal of Computational and Graphical Statistics 15(3), 502–523.
- Guinehut, S., A.-L. Dhomps, G. Larnicol, and P.-Y. Le Traon (2012). High resolution 3-D temperature and salinity fields derived from in situ and satellite observations. Ocean Science 8(5), 845–857.
- Haidvogel, D., H. Arango, W. Budgell, B. Cornuelle, E. Curchitser, E. Di Lorenzo, K. Fen-

- nel, W. Geyer, A. Hermann, L. Lanerolle, J. Levin, J. McWilliams, A. Miller, A. Moore, T. Powell, A. Shchepetkin, C. Sherwood, R. Signell, J. Warner, and J. Wilkin (2008). Ocean forecasting in terrain-following coordinates: Formulation and skill assessment of the regional ocean modeling system. Journal of Computational Physics 227(7), 3595–3624.
- Julier, S. J. and J. K. Uhlmann (1997). New extension of the kalman filter to nonlinear systems. In Signal processing, sensor fusion, and target recognition VI, Volume 3068, pp. 182–193. Spie.
- Kalman, R. E. (1960). A new approach to linear filtering and prediction problems. Journal of Basic Engineering 82(1), 35–45.
- Katzfuss, M., J. R. Stroud, and C. K. Wikle (2020). Ensemble kalman methods for high-dimensional hierarchical dynamic space-time models. Journal of the American Statistical Association 115(530), 866–885.
- Lei, L., D. R. Stauffer, and A. Deng (2012). A hybrid nudging-ensemble kalman filter approach to data assimilation. part ii: application in a shallow-water model. Tellus A: Dynamic Meteorology and Oceanography 64(1), 18485.
- Liang, X., X. Zheng, S. Zhang, G. Wu, Y. Dai, and Y. Li (2012). Maximum likelihood estimation of inflation factors on error covariance matrices for ensemble Kalman filter assimilation: MLE of inflation factors on error covariance matrices for EnKF. Quarterly Journal of the Royal Meteorological Society 138(662), 263–273.
- Lorenz, E. N. (1963). Deterministic nonperiodic flow. Journal of Atmospheric Sciences 20(2), 130 – 141.

- Lorenz, E. N. (1996). Predictability: A problem partly solved. In Proc. Seminar on predictability, Volume 1, pp. 1–18.
- Marchesiello, P., J. C. McWilliams, and A. Shchepetkin (2001). Open boundary conditions for long-term integration of regional oceanic models. Ocean Modelling 3(1), 1–20.
- Pailleux, J. (1990). A global variational assimilation scheme and its application for using tovs radiances. In Proc. WMO International Symposium on Assimilation of Observations in Meteorology and Oceanography, pp. 325–328.
- Qiu, Y. and S. X. Chen (2015). Bandwidth selection for high-dimensional covariance matrix estimation. Journal of the American Statistical Association 110(511), 1160–1174.
- Shchepetkin, A. F. and J. C. McWilliams (2005). The regional oceanic modeling system (roms): a split-explicit, free-surface, topography-following-coordinate oceanic model. Ocean Modelling 9(4), 347–404.
- Stroud, J. R., M. L. Stein, B. M. Lesht, D. J. Schwab, and D. Beletsky (2010). An Ensemble Kalman Filter and smoother for satellite data assimilation. Journal of the American Statistical Association 105(491), 978–990.
- Thepaut, J.-N. and P. Courtier (1991). Four-dimensional variational data assimilation using the adjoint of a multilevel primitive-equation model. Quarterly Journal of the Royal Meteorological Society 117(502), 1225–1254.
- Wang, X. and C. H. Bishop (2003). A comparison of breeding and ensemble transform Kalman filter ensemble forecast schemes. Journal of the Atmospheric Sciences 60(9), 1140–1158.